

Numerical computation of thermocapillary-driven convection in an open cylindrical cavity with different aspect ratios

SHOU-SHING HSIEH† and MAO-YU WEN

Department of Mechanical Engineering, National Sun Yat-Sen University, Kaohsiung, Taiwan 80424, R.O.C.

(Received 6 October 1992 and in final form 11 June 1993)

Abstract—The surface tension gradient driven fluid flow that occurs during laser melting has been studied. The steady laminar thermocapillary motion in a cylindrical cavity has been analyzed numerically for $0.01 \leq Pr \leq 20$, $50 \leq Re_\sigma \leq 35000$, $0.01 \leq A \leq 10$ without the inclusion of buoyancy effects. The study consists of scale analysis and numerical simulations. For a fixed Prandtl number the average free surface Nusselt number, side wall Nusselt number, bottom Nusselt number and maximum stream function are proportional to $Re_\sigma^{2/7}$, $Re_\sigma^{4/9}$, $Re_\sigma^{4/9}$, and $Re_\sigma^{-2/7}$, respectively. The numerical results are qualitatively verified by the scale analysis. The convection in the melt modifies the isotherms in the melt at high surface tension Reynolds number and Marangoni number. In addition, surface deflections are computed using a domain perturbation for small capillary number. It is shown that the degree of the free-surface deformation for the leading-order solution varies strongly with the surface tension Reynolds number.

1. INTRODUCTION

THE PRESENCE of a surface-tension gradient at the free surface between a liquid and a gas phase would influence the motion of these media. This induces fluid motion which is sometimes termed Marangoni convection or thermocapillary flow (for example, Yih [1] and Pearson [2]). The subject of thermocapillary convection has long been an area of interest due to complex flow patterns and practical applications. Studies on this subject range from the earlier fundamental understanding of Pearson [2] and Nield [3] to the more recent ones related to the materials processing problems such as crystal growth techniques (Chun [4], Schwabe and Scharmann [5]), welding and laser surface treatment (Kou and Sun [6]).

Bergman and Ramadhyani [7] simulated a convective flow in a square cavity driven by simultaneous buoyancy and thermocapillary effects. Usually, in the earth-gravity environment, such flows are overshadowed by natural convection (or forced convection), but at microgravity conditions, or when the dimension of the fluid system is small, their influences could be significant (see, for example, Bauer [8], Diezz [9], and Croll *et al.* [10]). An excellent numerical study of thermocapillary convection in square cavities was conducted by Zebib *et al.* [11]. They analyzed the structure of the flow by invoking ideas from boundary layer theory. In addition, the interface shape was calculated using a domain perturbation for small capillary numbers. Sen and Davis [12] reported an asymptotic solution of a steady thermocapillary flow in a shallow slot in which the interface shape was not flat.

Chen *et al.* [13] employed a finite-difference method with boundary-fitted technique to solve a steady thermocapillary free surface problem in a rectangular physical domain.

Although the thermocapillary flow induced by the temperature difference between the two vertical end walls in the rectangular cavity has been investigated, no effort has been made to study thermocapillary motion in an axisymmetric cylindrical cavity with free top that is heated along its top surface. The source of heat is modeled as a Gaussian distribution which is widely used in the laser surface working literature. In this paper the steady laminar thermocapillary motion in a cylindrical cavity with different aspect ratios (height to diameter) will be analyzed by a finite-difference procedure for $0.01 \leq Pr \leq 20$, $50 \leq Re_\sigma \leq 35000$, $0.01 \leq A \leq 10$. Moreover, in order to characterize the nature of stronger convection flows, the scale analysis is used to infer the boundary layer structure in the cavity for large but finite values of the surface tension Reynolds and Marangoni numbers. In addition, surface deflections are computed using domain perturbation for small capillary number ($Ca = A^3 \bar{Ca}$, $A \rightarrow 0$). It will be shown that, in some cases, thermocapillary flow can have remarkably strong influence on the flow field, temperature distribution, rate of heat transfer, and surface deflections in the cavity. Furthermore, the effect of the cylindrical geometry will be presented and compared with the previous investigations associated with a square cavity.

† Author to whom correspondence should be addressed.

NOMENCLATURE

A aspect ratio, W/D
Ca capillary number, $\gamma\Delta\theta A/\sigma_0$
 \overline{Ca} $O(1)$ for capillary number, Ca/A^3
D diameter of cylinder [m]
h deflection of the free surface [m]
h' thickness of the free surface boundary layer [m]
H dimensionless deflection of the free surface, h/W
k thermal conductivity [$W m^{-1} K^{-1}$]
l' thickness of the vertical side boundary layer [m]
Ma Marangoni number, $Re_\sigma Pr$
Nu local Nusselt number
 \overline{Nu} mean Nusselt number, $q'W/k\Delta\theta$
 \overline{Nu}_b mean Nusselt number of bottom wall
 \overline{Nu}_s mean Nusselt number of side wall
 \overline{Nu}_f mean Nusselt number of free surface
Pr Prandtl number, ν/α
P dimensionless pressure, $p/(\mu U_c D/W^2)$
 q_0 average heat flux applied at the free surface [$W m^{-2}$]
 $q(R)$ dimensionless heat flux distribution applied at the free surface, $\beta \exp(-\beta R^2)/(1 - \exp(-\beta))$
 q_R dimensionless heat flux distribution applied at the free surface, $q(R)/q_0$
R dimensionless radial coordinate, r/D
R₀ radius of cylinder [m]
Re_σ surface tension Reynolds number, $\rho U_c W/\mu$

T_0 temperature of rigid wall [K]
 ΔT characteristic temperature difference, $q_0 R_0/k$ [K]
 U_c characteristic velocity of fluid, $(d\sigma/dT)A(\Delta T/\mu)$ [$m s^{-1}$]
U dimensionless velocity in *z* direction, $u/U_c A$
V dimensionless velocity in *r* direction, v/U_c
W height of the cavity [m]
Z dimensionless axial coordinate, z/W

Greek symbols

α thermal diffusivity [$m^2 s^{-1}$]
 γ surface tension coefficient [$N m^{-2}$]
 δ_T thickness of the boundary layer [m]
 θ dimensionless temperature, $(T - T_0)/\Delta T$
 $\Delta\theta$ relative temperature with respect to the temperature T_0 [K]
 μ dynamic viscosity [$N s m^{-2}$]
 ν kinematic viscosity [$m^2 s^{-1}$]
 σ_0 an average surface tension over a range of radius of cylinder [$N m^{-1}$]
 κ curvature of free surface [m^{-1}]
 ψ stream function [$m^2 s^{-1}$]

Subscripts

c center of cavity
o leading order solution
1 second-order solution.

2. MATHEMATICAL FORMULATION

The simplified physical domain (Fig. 1) consists of a cylindrical cavity of diameter D and height W containing an incompressible, Newtonian liquid. The top horizontal boundary is a free surface exposure to a passive gas. The rigid, cold side wall and bottom wall are kept at a constant temperature T_0 . In addition, the

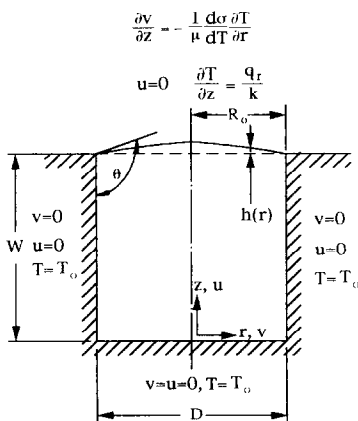


FIG. 1. Physical model of the present study.

following assumptions were made:

1. The system is steady, incompressible, laminar, axisymmetric, with constant properties and without viscous dissipation.
2. The solid-liquid interface shape (side wall) is at the melting point T_0 .
3. The buoyancy effect is ignored (see, for instance, Srinivasan and Basu [14]).
4. The thermal boundary condition on the free surface is modeled as a Gaussian distribution $q(R) = (\beta/1 - \exp(-\beta)) \exp(-\beta R^2)$ with $\beta = 5.0$.

According to the above assumptions and introducing the dimensionless variables, the governing equations can be written in following form:

$$\frac{\partial V}{\partial R} + \frac{V}{R} + \frac{\partial U}{\partial Z} = 0 \tag{1a}$$

$$Re_\sigma A \left(V \frac{\partial V}{\partial R} + U \frac{\partial V}{\partial Z} \right) = - \frac{\partial P}{\partial R} + A^2 \left(\frac{\partial^2 V}{\partial R^2} + \frac{\partial V}{\partial R} - \frac{V}{R^2} \right) + \frac{\partial^2 V}{\partial Z^2} \tag{1b}$$

$$Re_\sigma A^3 \left(V \frac{\partial U}{\partial R} + U \frac{\partial U}{\partial Z} \right) = - \frac{\partial P}{\partial Z} + A^2 \left(A^2 \frac{\partial^2 U}{\partial R^2} + A^2 \frac{\partial U}{\partial R} \frac{\partial R}{R^2} + \frac{\partial^2 U}{\partial Z^2} \right) \quad (1c)$$

$$MaA \left(V \frac{\partial \theta}{\partial R} + U \frac{\partial \theta}{\partial Z} \right) = A^2 \left(\frac{\partial^2 \theta}{\partial R^2} + \frac{\partial \theta}{\partial R} \frac{\partial R}{R} \right) + \frac{\partial^2 \theta}{\partial Z^2} \quad (1d)$$

The boundary conditions in dimensionless form can be given as follows:

$$U = V = \theta = 0; \quad \text{at } R = 0.5, \quad 0 < Z < 1 \quad (2a)$$

$$U = V = \theta = 0; \quad \text{at } Z = 0, \quad 0 < R < 0.5 \quad (2b)$$

$$U = \frac{\partial V}{\partial R} = \frac{\partial \theta}{\partial R} = 0; \quad \text{at } R = 0, \quad 0 < Z < 1 \quad (2c)$$

$$U = 0, \quad \frac{\partial V}{\partial Z} = \frac{\partial \theta}{\partial R};$$

$$\frac{\partial \theta}{\partial Z} = q(R) = \frac{\beta}{1 - \exp(-\beta)} \exp(-\beta R^2) \quad \text{at } Z = 1, \quad 0 < R < 0.5. \quad (2d)$$

3. SCALING AND STRUCTURE

Since the key to the correct correlation of seemingly complicated trends such as convection melting is the identification of the proper scales of the phenomenon, the scale analysis is made to infer the boundary layer

structure in the cylindrical cavity. According to the flow field of the present computation, the phenomenon consists of a sequence of four regimes: (a) free surface boundary layer, (b) core region, (c) corner region and, finally, (d) side wall boundary layer.

Due to the present driving force of the fluid mainly caused by the shear stress of the free surface, it would generate a main vortex near the upper corner at the side wall. This main vortex would enhance the secondary vortex at the lower corner as the surface tension Reynolds number increases until the vertical thermal layer at the side wall is developed completely. Thus a picture of the boundary layer structure might be developed as shown in Table 1. In addition, in order to simplify this scale analysis the necessary assumptions are made: (1) the main driving force of the fluid is caused by the shear stress of the free surface; (2) the surface tension Reynolds number and Marangoni number are large but finite values (5000–35 000 or so); (3) the flow is laminar, two-dimensional and axisymmetric; (4) the properties are all constant; (5) any particle on the free surface will remain on the free surface permanently; (6) the interface between the two immiscible fluids is sufficiently clean so as to avoid the convective instabilities.

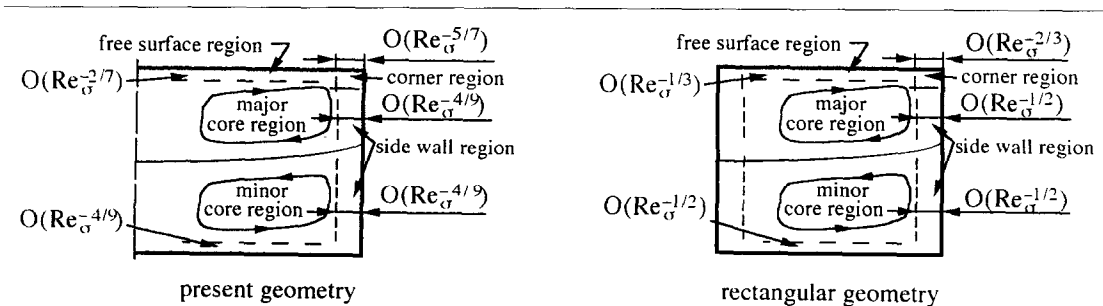
Considering the conservation of mass, momentum, and energy in the thermal boundary region ($R \approx O(1)$, $Z \approx \delta_T$) at free surface, where the driving force caused by the shear stress is strongly felt, the following shear stress balance is therefore established, $(\partial V / \partial Z) = -(\partial \theta / \partial R)$. The energy equation in the free surface layer expresses a balance between convection and conduction, namely,

Table 1. The scales of the relevant boundary layer regions

Regions	U		V		ψ		Nu	
	Present study	Zebib <i>et al.</i> [11]	Present study	Zebib <i>et al.</i> [11]	Present study	Zebib <i>et al.</i> [11]	Present study	Rectangular geometry
Free surface layer	$Re_\sigma^{-4/7}$	$Re_\sigma^{-2/3}$	$Re_\sigma^{-2/7}$	$Re_\sigma^{-1/3}$	$Re_\sigma^{-4/7}$	$Re_\sigma^{-2/3}$	$Re_\sigma^{2/7}$	$Re_\sigma^{1/3}$
Core region	$Re_\sigma^{2/7}$	$Re_\sigma^{-1/3}$	$Re_\sigma^{-2/7}$	$Re_\sigma^{-1/3}$	$Re_\sigma^{-2/7}$	$Re_\sigma^{-1/3}$	NA	NA
Corner region	1	1	$Re_\sigma^{-2/7}$	$Re_\sigma^{-1/3}$	$Re_\sigma^{-9/7}$	$Re_\sigma^{-2/3}$	NA	NA
Side wall layer	1	1	$Re_\sigma^{-4/9}$	$Re_\sigma^{-1/2}$	$Re_\sigma^{-8/9}$	Re_σ^{-1}	$Re_\sigma^{4/9}$	$Re_\sigma^{1/2}$

Note: NA stands for 'not available'

Sketch of the important boundary layer regions



$$\underbrace{V \frac{\Delta\theta}{l}}_{\text{Convection}}, \underbrace{U \frac{\Delta\theta}{\delta_T}}_{\text{Conduction}} \approx Re_\sigma^{-1} \frac{\Delta\theta}{\delta_T^2} \tag{3}$$

From the conservation of mass in the same region, that is, $(V/l) \approx (U/\delta_T)$, the two convection terms in equation (3) are of order $U(\Delta\theta/\delta_T)$. Thus, the energy balance becomes $V(\Delta\theta/l) \approx Re_\sigma^{-1}(\Delta\theta/\delta_T^2)$. Here, a modified thermal boundary layer thickness $\delta_T(R_o/\delta_T)^{1/4}$ was proposed to replace the initial δ_T . This is due to the curvature effect of the present physical geometry. Following Hsieh *et al.* [15] an amplification factor $(R_o/\delta_T)^{1/4}$ was introduced and it was not derived from the mathematics. It solely depends on the present numerical data and phenomenological behavior. This substitution yields $V \approx (Re_\sigma^{-1}/\delta_T^2)$. Now, turning our attention to the shear stress balance $(V/\delta_T) \approx (\Delta\theta/l)$, this results in $V \approx \delta_T$. Hence, one may obtain $\delta_T \approx Re_\sigma^{-2/7}$. Furthermore, the horizontal velocity length scale becomes $V \approx Re_\sigma^{-2/7}$. Finally, using the above energy balance, yields $U \approx Re_\sigma^{-4/7}$. The conventional definition of stream function results in $\psi \approx Re_\sigma^{-4/7}$. Since the length scale of heat transfer coefficient is k/δ_T , the average Nusselt number on the free surface can be written as

$$\overline{Nu} = \frac{hD}{k} \approx Re_\sigma^{2/7} \tag{4}$$

In the core region, the driving force is caused by the shear stress on the free surface. The velocity must match between the core and the free surface layer. Since $R, Z \approx O(1)$ in the core, and $V \approx Re_\sigma^{-2/7}$ in the free surface layer, and from matching condition, the horizontal velocity length scale in the core region should be $V \approx Re_\sigma^{-2/7}$. Using the conservation of mass in the core region, one may obtain $U \approx Re_\sigma^{-2/7}$, and so, the stream function is $\psi \approx Re_\sigma^{-2/7}$.

In the corner region, since the horizontal free surface flow turns in the corner region, the free surface velocity at $U(R, 1)$ would drop sharply to zero. The flux of fluid in this region is determined by the corresponding quantities in the free surface region. Thus, from the scaling of the free surface layer, one can find $V \approx Re_\sigma^{-2/7}, Z \approx Re_\sigma^{-2/7}$. Using the same analysis as equations (3) and (4) derived, these can result in $R \approx Re_\sigma^{-5/7}, U \approx O(1)$ and $\psi \approx Re_\sigma^{-9/7}$. For the side wall boundary layer, generally speaking, large velocities are confined to the free surface layer and the cold corner region for the thermocapillary flow, these in turn drive a core circulation. The flux of fluid in the boundary layer of the rigid wall can be determined by the corresponding quantities in the corner region. Thus $U \approx O(1)$. Let us set the following scales in the thermal boundary layer region: $R \approx \delta_T, Z \approx W$ and $\delta_T \ll W$. According to the similar derivation, finally, one may conclude the following results $V \approx \delta_T \approx Re_\sigma^{-4/9}, \psi \approx Re_\sigma^{-8/9}$ and $\overline{Nu} \approx Re_\sigma^{4/9}$.

The relevant scale of the present study and a comparison with Zebib *et al.* [11] was summarized in

Table 1. In the following, these scaling laws and flow features will be verified by means of a numerical simulation of the thermocapillary convection fluid flow.

4. FREE-SURFACE DEFLECTION FOR SMALL CAPILLARY NUMBER $Ca = \overline{Ca}A^3$

The capillary number Ca (which is a measure of the free surface deformation) in this study tends to be zero so that the free surface can be assumed to remain flat at leading order. For small capillary number, the surface deflection due to normal stresses generated by the flow is generally small, thus the formulation of the free-surface location given in the following may be obtained using a perturbation method.

$$\begin{aligned}
 -P + 2A^2 \left[1 + A^2 \left(\frac{dH}{dR} \right)^2 \right]^4 & \left[\left(\frac{\partial U}{\partial Z} - \frac{dH}{dR} \frac{\partial V}{\partial Z} \right) \right. \\
 & \left. + A^2 \frac{dH}{dR} \left(-\frac{\partial U}{\partial R} + \frac{dH}{dR} \frac{\partial V}{\partial R} \right) \right] \\
 = ACa^{-1} (1 - A^{-1}Ca\theta) & \left\{ \frac{d^2 H}{dR^2} / \left[1 + A^2 \left(\frac{dH}{dR} \right)^2 \right]^{3/2} \right. \\
 & \left. - \frac{dH}{dR} / \left[R \left(1 + A^2 \left(\frac{dH}{dR} \right)^2 \right) \right]^{1/2} \right\} \tag{5}
 \end{aligned}$$

In the derivation, following the procedure by Sen and Davis [12] for a square cavity, the limits of $A \rightarrow 0$ and $Ca = \overline{Ca}A^3$ are taken. The first-order correction for $O(A)$ to the surface deflection is then

$$\frac{d^2 H_1}{dR^2} - \frac{dH_1}{dR} \frac{1}{R} = -\overline{Ca}P_o \tag{6}$$

Considering the boundary conditions, the first-order correction to the surface deflection must satisfy

$$\begin{aligned}
 H_1(R)|_{R=0.5} = 0, \quad \frac{dH_1}{dR} \Big|_{R=0} = 0 \\
 \text{and} \quad \int_0^{0.5} RH_1(R) dR = 0. \tag{7}
 \end{aligned}$$

Equation (7) stands for the contact-line condition of the free surface for a fixed location, the axisymmetry and an additional constraint on $H_1(R)$ from global continuity, respectively. Thus $H_1(R)$ can be determined to $O(\overline{Ca})$ by solving equations (6) and (7) once P_o has been found.

5. NUMERICAL COMPUTATION

The SIMPLE (Semi Implicit Method for Pressure Linked Equation) method described by Patankar [16] with a slight modification will be applied to solve the aforementioned simultaneous differential equations (1a)–(1d). In this regard the calculation domain is subdivided into a number of rectangular control volumes. The governing differential equations are integrated over each control volume to obtain the finite-

difference equations involving variables U , V , P , and θ . Equations (1a)–(1d) can be rewritten in the conservative form

$$\frac{1}{R} \left[\frac{\partial}{\partial R} (VR\Phi) + \frac{\partial}{\partial Z} (UR\Phi) - \frac{\partial}{\partial R} \left(R\Gamma_{\phi R} \frac{\partial \Phi}{\partial R} \right) - \frac{\partial}{\partial Z} \left(R\Gamma_{\phi Z} \frac{\partial \Phi}{\partial Z} \right) \right] = S_{\phi} \quad (8)$$

where the first two terms on the LHS of equation (8) are the convection terms, the last two terms on the LHS of equation (8) are the diffusion terms, and the term on the RHS is the source term. The dependent variable Φ stands for a variety of different quantities. Besides, $\Gamma_{\phi R}$ (or $\Gamma_{\phi Z}$) and S_{ϕ} are specific to a particular meaning of Φ . Line inversion iteration with a relaxation value of 0.5 for velocity terms and 0.8 for the pressure correction term were used to facilitate calculation. A variable Φ is said to have converged if the following criterion is satisfied for all grid points (i, j) :

$$\left| \frac{\Phi_{i,j}^{n+1} - \Phi_{i,j}^n}{|\Phi_{i,j}^n|} \right|_{\max} \leq \varepsilon \quad (9)$$

where n stands for the n th iteration and ε was set to 10^{-5} .

A nonuniform scheme with an exponential grid generation was used so that the meshes graded toward the side and bottom walls and toward the free surface. The grid size effect has been examined by comparing the results obtained with various different nonuniform grid systems. The solution can be confirmed by two measures which are invariant to mesh refinement and global heat conservation. Since no heat is lost from either the free surface at $Z = 1$ or the side (or bottom) wall, the Nusselt number must be satisfied for the exact solution. The computations with three grid schemes (21×41 , 31×61 and 41×81) yielded almost identical results (only a 0.3% change in maximum stream function and less than 0.5% for the average Nusselt number), and it coincides energy balance within 0.2%. In addition, details about the grid influence on the main characteristics of the flow and heat transfer (the velocity and temperature distributions at the free surface) are computed with three different grids shown in Fig. 2. The coarse 21×41 (horizontal by vertical) grid with the smallest size of 0.0063 was not adequate. The 41×81 grid with the smallest spacing of 0.0017 was considered to be acceptable for both cases. For the surface velocity distribution, it has a spike near the cold wall due to thermocapillary flow driven by a sharp temperature gradient in that region. As discussed by Chen [17], an accurate numerical scheme with a very fine grid system is needed to resolve the cold corner region accurately at high Ma . At $Ma > 40\,000$ in the present work the corner region is not accurately resolved by 41×81 system and the peak value would increase with a finer grid. This value ($Ma = 40\,000$) is different from the result ($Ma =$

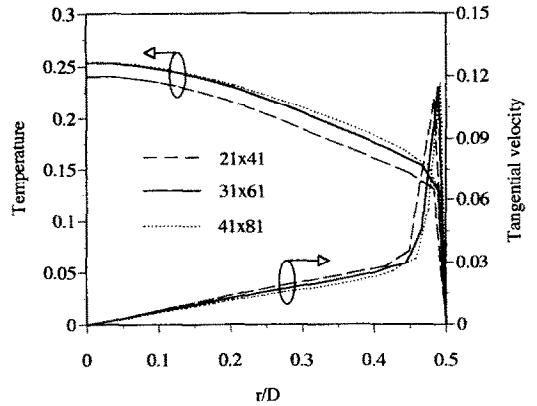


FIG. 2. Surface velocity and temperature distributions computed with various grid systems ($Pr = 1.0$, $Re_{\sigma} = 10\,000$, $A = 1.0$).

7000) discussed by Kamotani and Platt [18]. This difference may be due to the curvature effect of present cylindrical geometry. Furthermore, it is found that no convergent solution can be obtained for 41×81 grid system at $Ma > 1 \times 10^7$ and it presents nonmonotonic dependence on the Marangoni number for $Pr \leq \sim 15$. This is slightly in agreement with the results discussed by Carpenter and Homsy [19] due to different physical geometry. The nonuniform 41×81 grid is adopted for the general case of present numerical computation. All computing details are shown in Table 2.

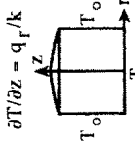
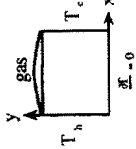
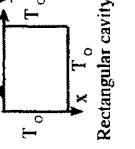
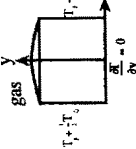
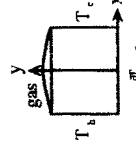
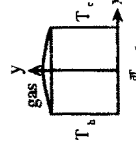
6. RESULTS AND DISCUSSION

In Table 2, the results of the present study are compared with the previous investigations of the thermocapillary-driven convection. This table was applied to provide a basis for the assessment of the various methods and results calculated. From the previous studies of the thermocapillary-driven convection, it is found that the thermocapillary flows are governed by four parameters, Re_{σ} , A (aspect ratio), \overline{Ca} and Pr ($Ma = Re_{\sigma}Pr$). This can also be seen from equations (1a)–(1d) and (6). The numerical results are presented herein for $0.01 \leq Pr \leq 20$, $50 \leq Re_{\sigma} \leq 35\,000$, $0.01 \leq A \leq 10$, $10 \leq \overline{Ca} \leq 25$ ($Pr = 0.1$: typical molten metals like iron, $Pr = 1$: substances like chloride, and $Pr = 20$: typical non-metals like silicon). The following representative results were extracted from the original data to illustrate this surface tension-driven fluid flow.

6.1. Temperature and flow fields

Figures 3(a)–(d) show the isotherm patterns (left) and streamline patterns (right) with $Pr = 1$ for surface tension Reynolds numbers of 500, 2000, 5000 and 10 000, respectively. Due to the resolution of the computer plot, several streamlines shown have a little bit of overlap in certain portions in Fig. 3 which is not the actual condition. In Figs. 3(a)–(d) (right), the flow patterns exist as two vortices in half of the cavity for present study, one located in the clockwise (CW) at

Table 2. Comparison with the previous investigations of the thermocapillary driven convection

Authors	Physical model	Method	Mesh	Range of relative parameters	Influence of gravity	Interface shape	Comments
This study	$\partial T/\partial z = -q_r/k$  Cylindrical cavity	FDM: modified SIMPLE Domain perturbation ($A \rightarrow 0, Ca = A^3 Ca$) Scale analysis	Nonuniform (exponential form): 41×81 for general case (According to the variety of Re_σ values, the exponent is used from 0.7-0.9 and 1.2-1.4)	$50 \leq Re_\sigma \leq 35000$ $0.01 \leq Pr \leq 20$ $0.01 \leq A \leq 10$ $10 \leq Ca \leq 25$	No	Nearly flat	For 41×81 grid, $A = 1$ 1. At $40000 < Ma < 100000$ the finer grid systems are needed. 2. No convergent solution at $Ma > 1 \times 10^5$.
Chen <i>et al.</i> [13]	 Rectangular cavity	FDM: PCMI	Nonuniform (boundary fitted curvilinear coordinate system) 61×21 for $A = 0.2$; also 41×41 for $A = 1$	$1 \leq Re_\sigma \leq 8500$ $0.2 \leq Pr \leq 50$ $0.2 \leq A \leq 1$ $0 \leq Ca \leq 0.32$ $0.2 \leq Ma \leq 1$ $Bi = 1$	No	Not flat	An initial shape of the gas-liquid interface must be chosen.
Srinivasan and Basu [14]	$T = T_0 + (T_c - T_0) \sin^2 \frac{\pi y}{H}$ Free surface  Rectangular cavity	FDM: ADI; Second upwind-differencing for convection terms	Uniform (?) 41×41	$100 \leq Re_\sigma \leq 10000$ $0.1 \leq Pr \leq 10$ $0.2 \leq A \leq 5$	No	Flat	1. Stability criteria: $\Delta t^* < 0.0008 Re_\sigma / A, Re_\sigma > Ma$ $\Delta t^* < 0.0008 Ma / A, Re_\sigma < Ma$. 2. Solution at $Re_\sigma > 1750$ resulted in very slow convergence using the central-difference scheme.
Zebib <i>et al.</i> [11]	 Rectangular cavity	FDM: SIMPLE; Domain perturbation ($Ca \rightarrow \infty$) Scale analysis	Nonuniform: 62×54 and 70×60 Uniform: 65×65 and 80×80 Nonuniform: $64 \times 64, 74 \times 74$ and 84×84	$20 \leq Re_\sigma \leq 50000$ $0.1 \leq Pr \leq 50$ $A = 1$	No	Nearly flat ($Ca \rightarrow 0$)	1. Solution at $Re_\sigma \approx 10^4-10^5$ is not steady. 2. Estimates error $< 3\%$ at $Re_\sigma \leq 5 \times 10^4$.
Carpenter and Homay [18]	 Rectangular cavity	1. Theoretical method: Asymptotic method ($A \rightarrow 0, Ca = A^4 Ca$, $Re_\sigma = A Re_\sigma, Ma = A Ma$, and $Bi = O(1)$). 2. FDM: 13-point finite-difference approximation of the biharmonic operator and a 5-point approximation of the Laplacian.	(?)	$0.1 \leq Pr \leq 50$ $0.2 \leq A \leq 1$ $5 \leq Ca \leq 20$	No	Not flat	1. Solution is highly sensitive to Ma at $Ma > 1 \times 10^5$, $1 \leq Pr \leq 50$. 2. Solution presents nonmonotonic dependence on Ma for $Pr \leq \sim 10$.
Sen and Davis [12]	 Rectangular cavity						

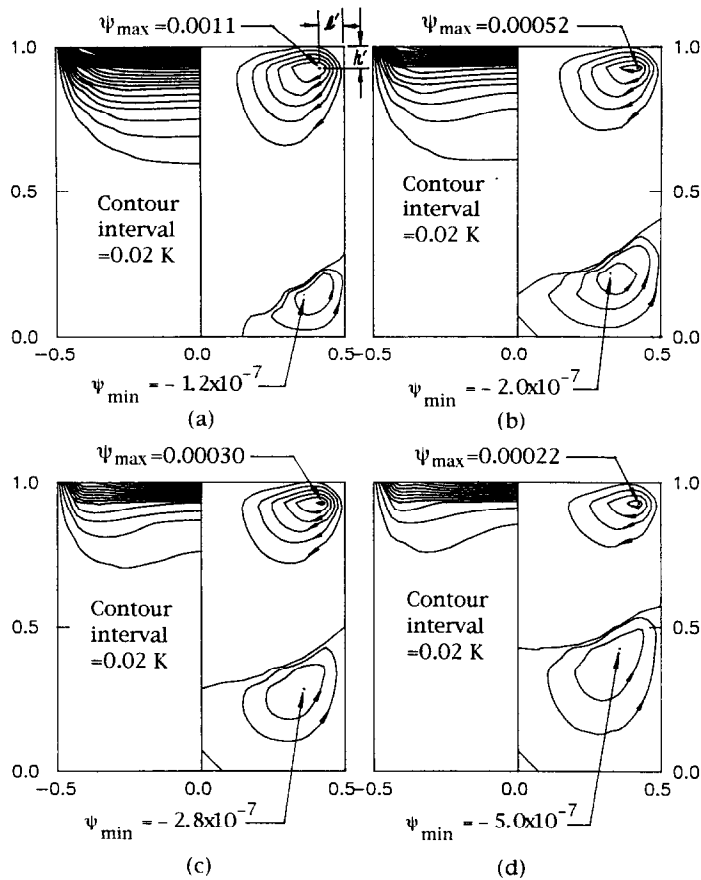


FIG. 3. Isotherms (left) and streamlines (right) for (a) $Re_s = 500$, (b) $Re_s = 2000$, (c) $Re_s = 5000$, (d) $Re_s = 10000$.

the upper domain, other located in the counter-clockwise (CCW) at the lower domain. The CW vortex stands for the stream function of positive value. On the contrary, the CCW vortex expresses the stream function of the negative value. It is found that the vertical jet driven by surface tension in the boundary-layer region is accelerated downward on the right side and leftward simultaneously and discharges into a pool of the nearly isothermal trapped fluid. Meanwhile, the fluid jet is decelerated and carries the secondary vortex at the corner of the bottom up to the half height of the cavity. There, the fluid loses much of its momentum before smoothly rounding the lower left-hand corner of the major cell. Then, the hot fluids near the center of the cavity are moved upward due to the action of the surface tension. On the other hand, when the stronger CW vortex loses much of its momentum, it causes another fluid jet near the CW vortex at the lower domain accelerated leftward and downward simultaneously, and finally, discharges into another pool of the nearly isothermal trapped fluid. As the flow jet approaches the bottom surface gradually, these fluids are decelerated. Then, due to the action of the stronger CW vortex, it is carried to turn rightward and upward simultaneously. These motions are continuous and repeated. The secondary,

weaker CCW vortex is therefore formed. Moreover, it is also found that the flow is clearly driven by the surface tension and the flow consists of a major cell, accompanied by a secondary cell at the lower domain. This phenomenon becomes more and more obvious as the surface tension Reynolds number increases. When the surface tension Reynolds number is 500 (Fig. 3(a)), one cell fills the lower corner of the cavity. If the surface tension Reynolds number reaches 2000 (Fig. 3(b)), the secondary cell has occupied the bottom of the cavity. This behavior persists until the surface tension Reynolds number is 10000 (Fig. 3(d)) at which the secondary cell at the bottom of the cavity becomes the same size as the major cell at the top of the cavity. However, there is a rapid change for both size and strength in the flow pattern as Re_s increased from 500 to 5000 (from Fig. 3(a) to (c)). No substantial change from 5000 to 10000 (Fig. 3(c) to (d)) was noted. This is because the major vortex moves these fluids near the corner of the bottom to yield the secondary vortex at early stage ($Re_s < 500$). When the minor CCW vortex is formed and since the drag force of the stronger CW vortex in the upper domain is larger than another one in the lower domain, the CCW vortex is moved upward to the stronger CW vortex until the Re_s reaches 5000. When $Re_s > 5000$,

an increase of Re_σ would enhance the strength of the CCW vortex in the lower domain. This can be seen from the slow reduction of the ψ_{\max} values of the stronger CW vortex, while the ψ_{\min} values of the CCW vortex increases quickly in this stage. Moreover, the free surface boundary layer is most evident in the upper section of height h' , where it is sandwiched by the most pronounced temperature difference $\Delta\theta$. When Re_σ increases, the major vortex becomes weaker as evidenced by the values of ψ_{\max} . Taking a closer examination of Fig. 3, it also indicates that the thickness of the free surface layer is almost constant ($h' \approx 0.10$ at $R = 0.25$) as the surface tension Reynolds number increased from 500 to 10000. In addition, the variations of the thickness of the vertical layer for the surface tension Reynolds number from 500 to 5000 can be also obtained ($l' \approx 0-0.16052$ at $Z = 0.5$). However, it is found that the thickness of vertical layer has no substantial change for the surface tension Reynolds number from 5000 to 10000 ($l' \approx 0.19021$ at $Z = 0.5$).

Figures 3(a)–(d) (left) show the isotherms corresponding to the flows discussed in the preceding section for a fluid with Prandtl number $Pr = 1$ and surface tension Reynolds number ranged from $500 \leq Re_\sigma \leq 10000$. It is shown that, since the magnitude of the heat flux there is larger than anywhere else in the cavity, the isotherms near the top-center of the cavity are closer together. In addition, the fluid temperature at the center of the cavity surface is hotter than that of the side wall. Thus the surface tension of the fluid near the center of the cavity surface is lower than that near the side wall. Owing to the temperature gradient along the top surface, thermocapillary forces cause a shear force in the interior fluid. Thus the fluid is drawn along the surface from the center to the side wall. This is also the reason that the major CW vortex is formed in the upper corner. Besides, it is found that the isotherms are packed closer to the side wall due to the two vortices existing at the top and bottom right corners. This also explained the reason why very fine grids have to be clustered near the side wall and free surface to obtain reliable and accurate results. Conversely, on the bottom wall the temperature gradients are milder and the fluid temperature near the bottom-center of the cavity is higher than that of the side wall. This is because the vortex is both weaker and CCW (these can be seen in Fig. 3 (right)). Similarly, the isotherms of $T < 0.02$ are very close to the vertical walls, which also look like being coincident with the vertical walls. It indicates that the surface layers are extremely thin. Further inspection of Fig. 3 (left), shows that when the surface tension Reynolds number increases, the three boundary layers (free surface boundary layer, side wall boundary layer, and bottom boundary layer (see Table 1)) become more distinct. This is due to the free surface boundary layer being most evident in the region of the height h' where the core temperature is quite different from that of the free surface. The core is there thermally stratified.

The stratification again is most pronounced in the horizontal boundary layer of height h' . Furthermore, when the surface tension Reynolds number is less than 2000 the isotherm patterns are governed by conduction and, consequently, the thermocapillary convection plays a minor role. As the surface tension Reynolds number reached 5000 the thermocapillary convection begins to affect the isotherm patterns near the side wall of the cavity (see Fig. 3(a) (left)).

Figures 4(a)–(c) illustrate the isotherm patterns (left) and streamline patterns (right) with $Re_\sigma = 2500$ for $Pr = 0.1, 1.0$ and 20 , respectively, in which they show how the flow field responds to the diminishing temperature gradient over the central portion of the free surface as the Prandtl number is increased. It is also found that the strength in the flow pattern is decreased as Pr increased, and the isotherm patterns show a sensitive dependence on Pr . When $Pr \leq 1.0$ at this value of Re_σ , the isotherm patterns are mainly governed by conduction. As $Pr = 20$, the isotherm patterns are dominated by thermocapillary convection.

Isotherms and streamlines predicted for cavities with aspect ratios of 0.1, 0.5, 1.0, and 2.0 are shown in Figs. 5(a)–(d), respectively. As is evident, the surface tension-driven convection cell exists in all cases. The center of the surface tension cell rotation is at nearly the same vertical location, but the ψ_{\max} values are enhanced as aspect ratio increased. However, the flow patterns located on the upper side of the calculation domain seem independent of the variation of aspect ratio. On the other hand, the thermal field is stratified fairly linearly in the vertical direction in most of the flow domain. Further inspection of Figs. 5(a)–(d) (left) reveals that the isotherm initially (at $A = 0.1$) behaves as stratified and, later, it becomes a plume displayed. This plume becomes more pronounced as the aspect ratio increased.

6.2. Surface temperature and velocity profiles

Figure 6 shows how the dimensionless surface temperature and tangential velocity behave near the side wall for given Prandtl numbers and aspect ratios. The surface temperature distribution given in Fig. 6(a) shows that it becomes more uniform in the entire region as the Pr increased and the aspect ratios decreased except in the cold corner region. This surface temperature distribution coincides with the Gaussian distribution of present heat source on the free surface. In addition, in Fig. 6(b), the surface velocity increases monotonically from zero and drops back smoothly to zero in a small boundary layer next to the wall due to the effect of the endwall. It is therefore concluded that the influence of the vortex at the upper corner is quite important. The surface velocity profiles have one peak near the cold wall due to thermocapillary flow driven by a sharp temperature gradient in that region, which increases in magnitude and is located further away from the wall as Prandtl

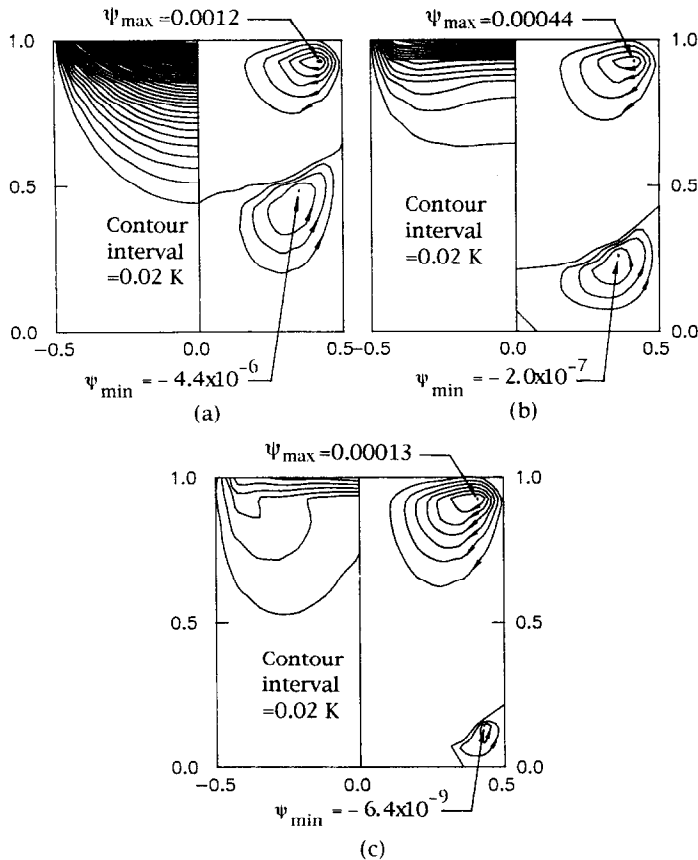


FIG. 4. Isotherms (left) and streamlines (right) for different Prandtl numbers with $A = 1$ and $Re_e = 2500$, (a) $Pr = 0.1$, (b) $Pr = 1.0$, (c) $Pr = 20$.

numbers decreased and aspect ratios increased, but the peak value is slightly reduced at Pr less than 0.1.

6.3. Heat transfer coefficient

The local Nusselt numbers for the side wall and bottom wall are defined as follows:

$$Nu_s = AZ \left. \frac{\partial \theta}{\partial R} \right|_{R=0.5} \quad Nu_b = \frac{R}{A} \left. \frac{\partial \theta}{\partial Z} \right|_{Z=0}$$

In Fig. 7(a) the local Nusselt number distributions on the side wall are shown. As expected, heat transfer at the lower half of the side of the cavity is affected only slightly by surface tension effects. In order to investigate the correlations between the heat transfer rate and the flow patterns in certain detail, part of the original drawing of the plot shown in Fig. 7(a) is enlarged. When the surface tension Reynolds number $Re_e \leq 10000$, the Nusselt number decreased as Re_e increased due to pure conduction at this stage as mentioned earlier. When $Re_e > 10000$, the Nusselt number increased as Re_e increased. This is because the thermocapillary convection begins to strongly influence the isotherm patterns. At the region where the major vortex exists the Nusselt number is increased substantially. The maximum Nusselt number along the side wall occurred near the top surface. This is

because of the surface tension effects, which are responsible for making the isotherms flat near the free surface as depicted earlier in Fig. 3, and this leads to rapid increases of Nu in the upper corner by surface tension-driven flow.

Surface tension effects are, of course, most pronounced at the free surface and become less important near the lower half of the side of the cavity. Nusselt number distributions at the bottom of the cavity are shown in Fig. 7(b). It is found that an increase in heat transfer is accompanied by a decrease of surface tension Reynolds number. Maximum values of Nu occur at the quarter span of the bottom surface (measured from the side wall) and they are associated with the secondary vortex fluid motion in the cavity. Although there is a vortex in the lower half region, the effect seems so small that the pure conduction was dominated. Therefore, the local Nusselt number does not exhibit a large change at the lower corner. Consequently, as also discussed earlier, the total heat transfer between the lower half side wall and bottom of the cavity is not significantly affected by thermocapillary-driven fluid flow.

The average Nusselt number of the side wall is obtained by integration of the local Nu which is given in the following:

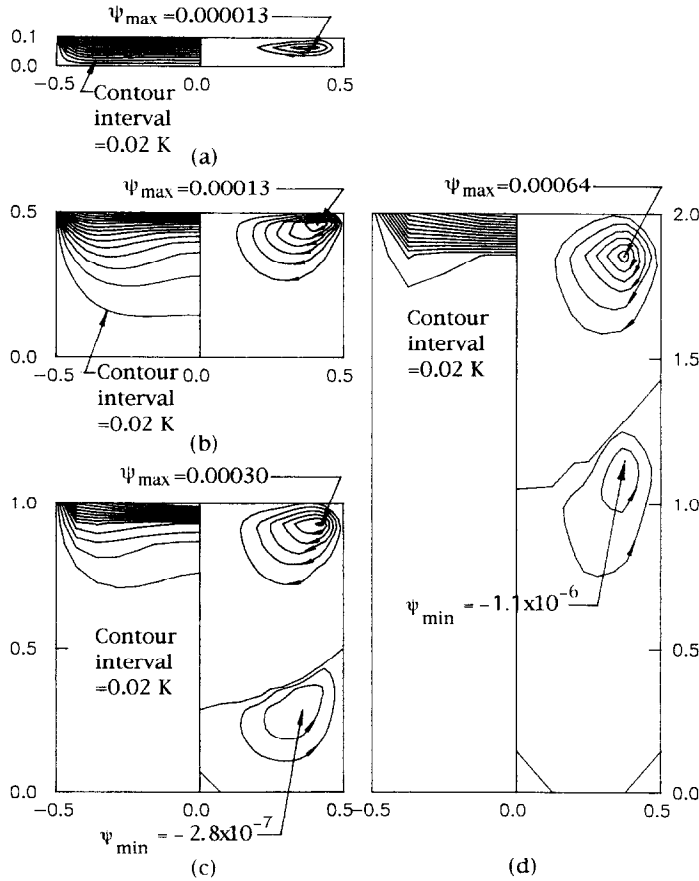


FIG. 5. Isotherms (left) and streamlines (right) for different aspect ratios with $Pr = 1.0$ and $Re_\sigma = 5000$, (a) $A = 0.1$, (b) $A = 0.5$, (c) $A = 1.0$, (d) $A = 2.0$.

$$\overline{Nu}_s = \frac{A}{H} \int_0^1 \left. \frac{\partial \theta}{\partial R} \right|_{R=0.5} dZ.$$

These Nusselt numbers will be discussed with scale analysis in the next section.

6.4. Comparison with numerical results and scale analysis

The scale analysis imposed herein may now be used for verification of the present numerical results. In Fig. 8 is shown a plot of maximum stream function and the average Nusselt numbers of the side wall for the case with $Pr = 1$. It is found that the results of maximum stream function for large but finite Re_σ ($Re_\sigma \approx 50-35\ 000$) are in good agreement qualitatively (the trend is the slope of $-2/7$) with those based on the asymptotic scaling in the core region. Moreover, it is also shown that the average Nusselt numbers of side wall increases as Re_σ increases when $Re_\sigma \ge 1000$. The results calculated for large but finite Re_σ ($\approx 1000-35\ 000$) fit the scaling law derived in Section 3 in the following functional form, $\overline{Nu}_s \approx Re_\sigma^{4/7}$.

Following Zebib *et al.* [11], the maximum strength of the circulation would occur in the core region with the magnitude of $\psi \approx O(Re_\sigma^{-1/3})$ which is slightly

different from the results $\psi_{max} \approx O(Re_\sigma^{-2/7})$ of the present study for the cylindrical geometry. The average Nusselt numbers of the side wall were also different from the results obtained by Zebib *et al.* [11] (see Fig. 8). These may be due to curvature effects of the present study. In addition, the overall boundary layer behavior (the surface boundary layer, the side wall boundary layer and the bottom boundary layer) is found to be not completely developed until the surface tension Reynolds number reaches 5000. When the surface tension $Re_\sigma > 5000$, it is suggested that a schematic summary of the structure could be given for $Pr = 1$ as shown in Table 1.

6.5. Free-surface deflections

The free surface deflection was calculated using a domain perturbation for small capillary numbers. In order to compare the present results with the asymptotic solution (Sen and Davis [12]) and the numerical solution (Chen *et al.* [13]), Table 3 was thus established.

Table 3 shows the free surface deflections for the height of a contact line fixed at $Z = A$ with $Re_\sigma = 1$, $Ma = 0.2$, $A = 0.2$. The results for a shallow cavity

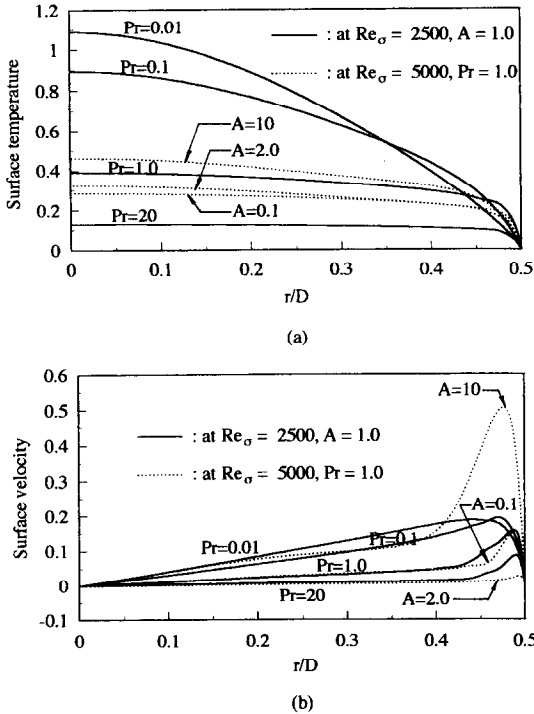


FIG. 6. (a) Surface temperature distributions, (b) surface velocity distributions for indicated Prandtl numbers and aspect ratios.

with small capillary, Reynolds, and Marangoni numbers are in good agreement with the previous asymptotic results (Sen and Davis [12]) and numerical results (Chen *et al.* [13]). Moreover, this strongly indicates

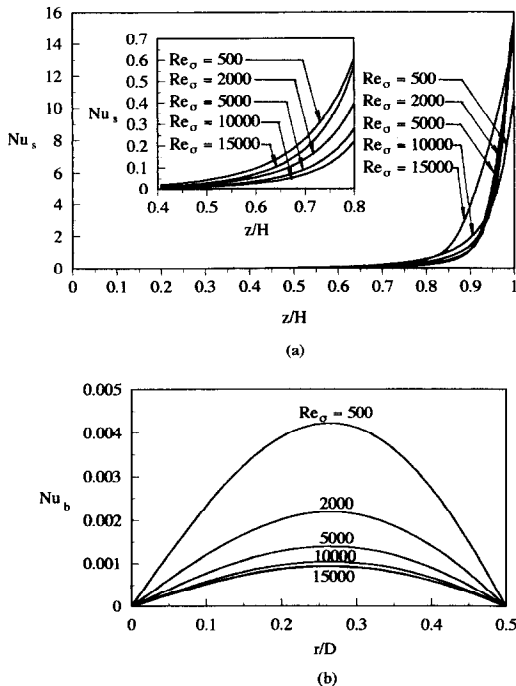


FIG. 7. Local Nusselt number distributions for various Re_σ , with $Pr = 1$, (a) side wall, (b) bottom wall.

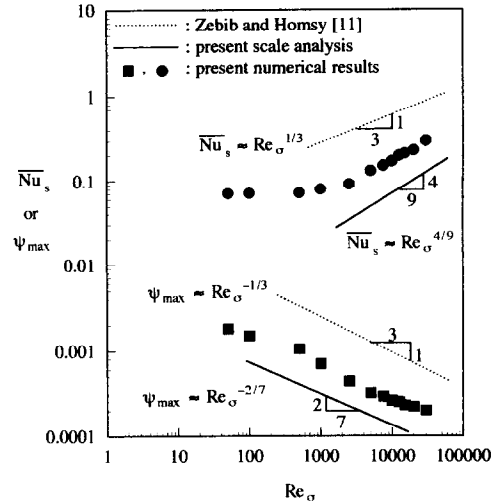


FIG. 8. Variation of Re_σ vs ψ_{max} and Nu_s .

that the free surface deflection at the leading order $O(A)$ is almost equal to the integrated free surface deflection. Hence, for small capillary numbers the free surface deflection can be estimated using a domain perturbation rather than other methods to save much computational time for iterative process.

The interfacial shape front distributions for various Reynolds numbers and capillary numbers are shown in Figs. 9(a) and (b), respectively. It is found that the free surface deflections have three peaks and two valleys. In addition, the free surface deflections have a minimum peak at the center and a maximum peak near the side wall. This is because the major vortex near the top corner decelerates the fluid from a certain maximum value to zero (also see Fig. 6). It can be seen that the leading order velocity and pressure determine the free surface deflection from the inspection of equations (6) and (7). Hence, the fluid pressure is increased from a lower value to a maximum value near the side wall. This high pressure forces the fluid to rise upward. In Fig. 9(a), the peaks of the surface deflection near the corner move toward the side wall with an increase of Re_σ . This is because the rotating point of the major vortex moves toward the top corner gradually with an increase of Re_σ (see Fig. 3 (right)). Moreover, on further increase of Re_σ (see Fig. 9(a)) or further decrease of \overline{Ca} (see Fig. 9(b)), the depression on the free surface becomes flatter due to the further increase of the surface tension. Further inspection of Fig. 9(a) shows that a boundary layer regime on the top was developed for Re_σ greater than about 5000. This can be also verified by the associated flow pattern shown an early plot in Fig. 3 (right).

7. CONCLUSIONS

Scale analysis, numerical simulation, and domain perturbation ($A \rightarrow 0, Ca = A^3 \overline{Ca}$) for surface deflec-

Table 3. Comparison with Sen and Davis [12], and Chen *et al.* [13] for free-surface deflection subjected to $Re_\sigma \approx 1$, $Ma = 0.2$, $A = 0.2$

\overline{Ca}	Numerical solution at the leading order for present study		Asymptotic solution at the leading order by Sen and Davis [12]		Numerical solution by Chen <i>et al.</i> [13]	
	$\min(AH_1(R))$	$\max(AH_1(R))$	$\min(AH_1(x))$	$\max(AH_1(x))$	$\min(H(x))$	$\max(H(x))$
5	-0.011	0.013	-0.012	0.012	-0.012	0.012
10	-0.022	0.025	-0.024	0.024	-0.024	0.024
15	-0.035	0.039	-0.036	0.036	-0.038	0.037
20	-0.046	0.051	-0.048	0.048	-0.053	0.050
Comments	$H(R) = 1 + AH_1(R) + O(A^1) = h(r)/W$		$H(x) = 1 + AH_1(x) + O(A^2) = h(x)/W$		$H(x) = h(x)/W$	

Physical geometry
Cylindrical cavity

Rectangular cavity

Rectangular cavity

tions were performed for the thermocapillary flow in a cylindrical cavity with free top during laser melting without the inclusion of buoyancy effect. Flow field, temperature distributions, heat transfer rates, asymptotic scalings, and surface deflections observed in this study lead to the following conclusions:

1. The temperature field is strongly influenced by

convection if the surface tension Reynolds number is large (say, $Re_\sigma \geq 2000$).

2. Surface tension effects are, of course, most pronounced at the free surface and become less influential near the lower half of the side of the cavity.

3. As Re_σ reached 5000, the horizontal boundary layer has almost developed ($h' \approx 0.10$ at $R = 0.25$). The thermocapillary convection begins to influence the isotherm patterns near the side wall. Furthermore, the major vortex continues to move the secondary vortex upward. The overall boundary layer behavior is not developed completely until Re_σ reached 5000 ($l' \approx 0.1902$ at $Z = 0.5$). Thereafter, the present numerical results are in good agreement with the asymptotic scalings, and a schematic summary of the structure is obtained which is shown in Table 1. The curvature effect due to the present geometry can reduce the influence of the thermocapillary flow.

4. As Re_σ increases or \overline{Ca} decreases, the surface deflection distorts further from the plane $Z = A$.

5. The leading order velocity and pressure gradients (mainly the pressure) determine the deflection of the liquid-gas interfaces.

Acknowledgement—Constructive comments from the referees are gratefully appreciated. This work was performed on a CONVEX C3840 Super Computer at National Sun Yat-Sen University Computer Center.

REFERENCES

1. C. S. Yih, Fluid motion induced by surface tension variation, *Phys. Fluids* **11**, 477-480 (1968).
2. J. R. A. Pearson, On cellular convection induced by surface tension, *J. Fluid Mech.* **4**, 489-500 (1958).
3. D. A. Nield, Surface tension and buoyancy effects in cellular convection, *J. Fluid Mech.* **19**, 341-352 (1964).
4. C.-H. Chun, Marangoni convection in floating zone under reduced gravity, *J. Cryst. Growth* **48**, 600-610 (1980).
5. D. Schwabe and A. Scharmann, Some evidence for the existence and magnitude of a critical Marangoni number for the onset of oscillatory flow in crystal growth melts, *J. Cryst. Growth* **46**, 125-131 (1979).

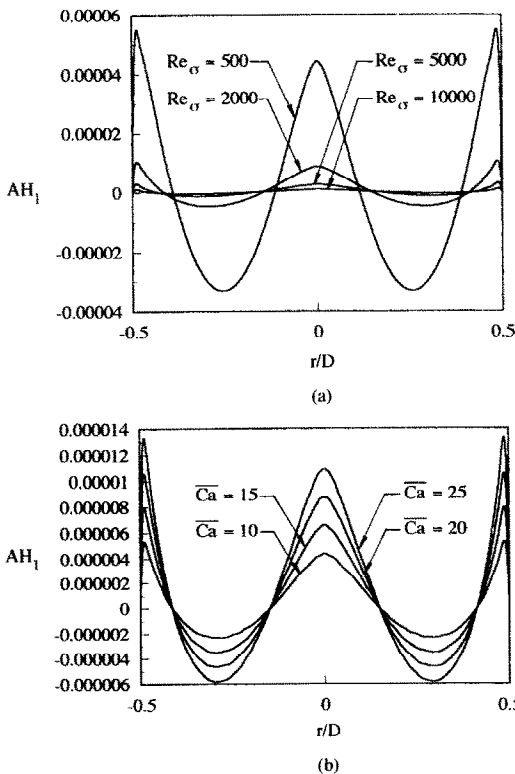


FIG. 9. Surface deflection vs (a) the various surface Reynolds number at $\overline{Ca} = 20$, (b) the various capillary number at $Re_\sigma = 2000$, for $A = 0.01$, $Pr = 1$ with a contact point $Z = A$.

6. S. Kou and D. K. Sun, Fluid flow and weld penetration in stationary arc welds, *Metall. Trans. A* **16**, 203–213 (1985).
7. T. L. Bergman and S. Ramadhyani, Combined buoyancy- and thermocapillary-driven convection in open square cavities, *Numer. Heat Transfer* **9**, 441–451 (1986).
8. H. F. Bauer, Heat transport in a liquid column in weightless conditions due to thermal Marangoni, *Numer. Heat Transfer* **8**, 81–97 (1985).
9. J. L. Diezz, Low-Marangoni low-Reynolds numbers capillary flow inside a slender liquid bridge, *Microgravity Sci. Technol.* **3**(4), 222–230 (1991).
10. A. Croll, W. Muller-Sebert, K. W. Benz and R. Nitsche, Natural and thermocapillary convection in partially confined silicon melt zones, *Microgravity Sci. Technol.* **3**(4), 204–215 (1991).
11. A. Zebib, G. M. Homsy and E. Meiburg, High Marangoni number convection in a square cavity, *Phys. Fluids* **28**, 3467–3476 (1985).
12. A. K. Sen and S. H. Davis, Steady thermocapillary flows in two-dimensional slots, *J. Fluid Mech.* **121**, 163–186 (1982).
13. J. C. Chen, J. C. Sheu and S. S. Jwu, Numerical computation of thermocapillary convection in a rectangular cavity, *Numer. Heat Transfer* **17**, 287–308 (1990).
14. J. Srinivasan and B. Basu, A numerical study of thermocapillary flow in a rectangular cavity during laser melting, *Int. J. Heat Mass Transfer* **29**, 563–572 (1986).
15. S.-S. Hsieh, W.-S. Han and S.-C. Lin, Natural convection of air layers in vertical annuli with cooled outer wall, *J. Thermophys.* **3**(2), 182–188 (1989).
16. S. V. Patankar, *Numerical Heat Transfer and Fluid Flow*. Hemisphere, New York (1980).
17. M. M. Chen, Thermocapillary convection in materials processing, *Interdisciplinary Issues in Materials Processing and Manufacturing*, ASME Vol. 2, pp. 541–558 (1987).
18. Y. Kamotani and J. Platt, Effect of free surface shape on combined thermocapillary and natural convection, *J. Thermophys. Heat Transfer* **6**(4), 721–726 (1992).
19. B. M. Carpenter and G. M. Homsy, High Marangoni number convection in a square cavity: Part II, *Phys. Fluids* **A2**, 137–149 (1990).